A&A 674, A129 (2023)
https://doi.org/10.1051/0004-6361/202245761

Astronomy & Astrophysics

Spatial metallicity variations of mono-temperature stellar populations revealed by early-type stars in LAMOST

Chun Wang[1], Haibo Yuan[2], Maosheng Xiang[3], Yuan-Sen Ting[4,5], Yang Huang[3], and Xiaowei Liu[6]

[1] Tianjin Astrophysics Center, Tianjin Normal University, Tianjin 300387, PR China
e-mail: wchun@tjnu.edu.cn
[2] Department of Astronomy, Beijing Normal University, Beijing 100875, PR China
e-mail: yuanhb@bnu.edu.cn
[3] National Astronomical Observatories, Chinese Academy of Sciences, Beijing 100012, PR China
[4] Research School of Astronomy and Astrophysics, Australian National University, Cotter Rd., Weston, ACT 2611, Australia
[5] School of Computing, Australian National University, Acton, ACT 2601, Australia
[6] South-Western Institute For Astronomy Research, Yunnan University, Kunming 650500, PR China

Received 22 December 2022 / Accepted 4 April 2023

ABSTRACT

We investigate the radial metallicity gradients and azimuthal metallicity distributions on the Galactocentric X–Y plane using mono-temperature stellar populations selected from the LAMOST-MRS young stellar sample. The estimated radial metallicity gradient ranges from −0.015 dex/kpc to −0.07 dex/kpc, which decreases as the effective temperature decreases (or when the stellar age increases) at $7500 < T_{\rm eff} < 12\,500$ K ($\tau < 1.5$ Gyr). The azimuthal metallicity excess (the metallicity after subtracting the radial metallicity gradient, Δ [M/H]) distributions exhibit inhomogeneities with dispersions of 0.04 dex to 0.07 dex, which decrease as the effective temperature decreases. We also identify five potential metal-poor substructures with large metallicity excess dispersions. The metallicity excess distributions of these five metal-poor substructures suggest that they contain a larger fraction of metal-poor stars compared to other control samples. These metal-poor substructures may be associated with high-velocity clouds that infall into the Galactic disk from the Galactic halo, which are not quickly well mixed with the pre-existing interstellar medium (ISM) of the Galactic disk. As a result, these high-velocity clouds produce some metal-poor stars and the observed metal-poor substructures. The variations of metallicity inhomogeneities with different stellar populations indicate that high-velocity clouds are not well mixed with the pre-existing Galactic disk ISM within 0.3 Gyr.

Key words. Galaxy: abundances – Galaxy: disk – Galaxy: evolution

1. Introduction

Metals in the interstellar medium (ISM) regulate its cooling process and the star formation of galaxies. The mixing process between infalling gas and the local ISM changes the fundamental properties, including the chemical abundance, of the local ISM and the future star formation process. Understanding the mixing process of the ISM is crucial for advancing our understanding of galaxy formation and evolution histories, such as Galactic archaeology and chemical evolution (Tinsley 1980; Matteucci 2012, 2021). Most studies thus far have assumed that the ISM is well mixed at a small scale.

The metallicity inhomogeneity of the ISM could help us to understand the ISM mixing. At a large scale, the ISM of the Galactic disk shows a negative radial metallicity gradient (Balser et al. 2011), suggesting an 'inside-out' disk formation scenario. At a small scale, the metallicity of the ISM (Balser et al. 2011, 2015; De Cia et al. 2021), Cepheid variable stars (Pedicelli et al. 2009; Poggio et al. 2022), open clusters (OCs; Davies et al. 2009; Poggio et al. 2022), young upper main-sequence stars (Poggio et al. 2022), and young main-sequence stars (Hawkins 2023) in the Milky Way (MW) present azimuthal metallicity variations. For other external spiral galaxies, researchers have also found azimuthal ISM metallicity variations (after subtracting the radial metallicity gradients) by studying the metallicity of H II regions (Ho et al. 2017, 2018; Kreckel et al. 2019, 2020). All of these observed azimuthal metallicity inhomogeneities of the MW and other spiral galaxies suggest that the ISM is not well mixed. To better understand the ISM mixing process, we need to explore the variations of metallicity inhomogeneity of the ISM over time, which has not been well studied yet.

Stellar surface chemical abundance almost remains unchanged during the main-sequence evolutionary stage. It is thus a fossil record of the ISM during the birth of these stars. The metallicity inhomogeneity of the ISM and its variations over time can be studied using a stellar sample with a wide age coverage. However, stars in the MW have moved away from their birth positions due to the secular evolution of the MW. Old stars have experienced stronger radial migration (Minchev & Famaey 2010; Kubryk et al. 2015; Frankel et al. 2018, 2020; Lian et al. 2022) compared to young stars. According to Frankel et al. (2018, 2020), 68% of stars have migrated within a distance of $3.6\sqrt{\tau/8\,\mathrm{Gyr}}$ kpc and $2.6\sqrt{\tau/6\,\mathrm{Gyr}}$ kpc, respectively. Hence, stars can move up ∼1 kpc within 1 Gyr. Lian et al. (2022) suggest that the average migration distance is 0.5–1.6 kpc at an age of 2 Gyr and 1.0–1.8 kpc at an age of 3 Gyr. In conclusion, young stars in the MW are valuable for studying the ISM mixing process due to their large sample size and wide age coverage compared to other young objects (e.g. OCs, Cepheid variable stars, H II regions) and because they are less affected by secular evolution compared to older stars. For young main-sequence stars, effective temperatures are tightly

correlated with stellar ages (Schaller et al. 1992; Zorec & Royer 2012; Sun et al. 2021). The variations of the ISM metallicity homogeneity (or inhomogeneity) over time can be investigated using a young main-sequence stellar sample with accurate determinations of stellar atmospheric parameters (effective temperature $T_{\rm eff}$, surface gravity $\log g$, and metallicity [M/H]).

Recently, accurate stellar atmospheric parameters were derived from medium-resolution spectra of Large Sky Area Multi-Object Fibre Spectroscopic Telescope (LAMOST) for 40 034 young (early-type) main-sequence stars (Sun et al. 2021). The stellar sample spans a wide range of effective temperatures (7500–15 000 K), and covers a large and contiguous volume of the Galactic disk. It allows us to investigate the ISM metallicity inhomogeneity and its variations over time. In this work, we investigate the radial metallicity gradients and azimuthal metallicity distribution features of mono-temperature stellar populations across the Galactic disk within $-10.5 < X < -8.0$ kpc, $-1.0 < Y < 1.5$ kpc, and $|Z| < 0.15$ kpc using the young stellar sample.

This paper is organised as follows. In Sect. 2, we introduce the adopted young stellar sample. In Sect. 3, we present the radial metallicity gradients of mono-temperature stellar populations. We present the azimuthal metallicity distributions of mono-temperature stellar populations in Sect. 4. The constraints on the ISM mixing process using the azimuthal metallicity distributions are discussed in Sect. 5. Finally, we summarise our work in Sect. 6.

2. Young stellar sample from the LAMOST Medium-Resolution Spectroscopic survey

2.1. Coordinate systems and Galactic parameters

Two coordinate systems are used in this paper. One is a right-handed Cartesian coordinate system (X, Y, Z) centred on the Galactic centre, with X increasing towards the Galactic centre, Y in the direction of Galactic rotation, and Z representing the height from the disk mid-plane, which is positive towards the north Galactic pole. The other is a Galactocentric cylindrical coordinate system (R, Φ, Z), with R representing the Galactocentric distance, Φ increasing in the direction of Galactic rotation, and Z the same as that in the Cartesian system. The Sun is assumed to be at the Galactic midplane (i.e. $Z_\odot = 0$ pc) and has a value of $R_\odot$ equal to 8.34 kpc (Reid et al. 2014).

2.2. Sample selections

As of March 2021, the LAMOST Medium-Resolution Spectroscopic (MRS) survey had collected 22 356 885 optical (4950–5350 Å and 6300–6800 Å) spectra with a resolution of $R \sim 7500$. Sun et al. (2021) selected 40 034 late B- and A-type main-sequence stars from the LAMOST-MRS survey (hereafter named the LAMOST-MRS young stellar sample) and extracted their accurate stellar atmospheric parameters. For a star with a spectral signal-to-noise ratio $S/N \sim 60$, the cross validated scatter is ~75 K, 0.06 dex, and 0.05 dex for $T_{\rm eff}$, $\log g$, and [M/H], respectively. We adopted the photogeometric distances provided by Bailer-Jones et al. (2021) for these stars. The X, Y, Z, R, and Φ of each star were estimated using its distance and coordinates, and the corresponding errors were also given using the error transfer function.

For the LAMOST-MRS young stellar sample, stars with $T_{\rm eff}$ and [M/H] uncertainties larger than 75 K and 0.05 dex were discarded to ensure the reliability of the results. Only stars with $7000 < T_{\rm eff} < 15\,000$ K, $\log g > 3.5$ dex, and $-1.2 <$ [M/H] < 0.5 dex were selected, as they are main-sequence stars with accurate metallicity determinations. Because young stars are mostly located in the Galactic plane, stars of $|Z| \geq 0.15$ kpc were also removed to reduce the contamination from old stars. Finally, our LAMOST-MRS young stellar sample consists of 14 692 unique stars. The stellar number density distribution on the X–Y plane is shown in Fig. 1.

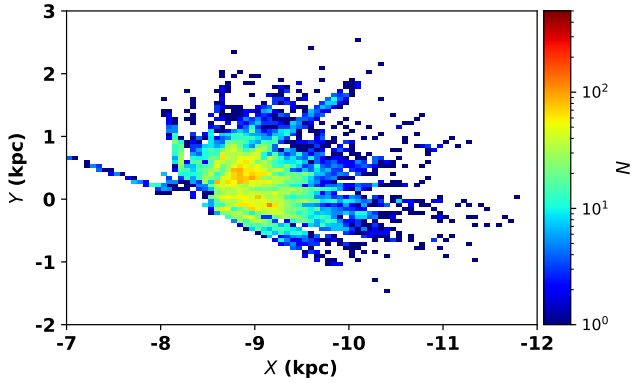

Fig. 1. Stellar number density distribution on the X–Y plane of the final LAMOST-MRS young stellar sample.

The faint limiting magnitude of the LAMOST-MRS is $g \sim 15$ mag. The faintest stars in the four effective temperature bins (adopted in the following context) have absolute g-band magnitudes of ~4.5 mag ($7500 < T_{\rm eff} < 8000$ K), ~4.0 mag ($8000 < T_{\rm eff} < 8500$ K), ~3.5 mag ($9500 < T_{\rm eff} < 10\,500$ K), and ~3.2 mag ($10\,000 < T_{\rm eff} < 12\,500$ K). Based on the distance modulus, stellar samples with $7500 < T_{\rm eff} < 8000$ K, $8000 < T_{\rm eff} < 8500$ K, $9500 < T_{\rm eff} < 10\,500$ K, and $10\,000 < T_{\rm eff} < 12\,500$ K are incomplete at distance $(d) > 1.258$ kpc, $d > 1.584$ kpc, $d > 1.955$ kpc, and $d > 2.29$ kpc, respectively.

2.3. Correcting for the $T_{\rm eff}$-metallicity systematics caused by a NLTE effect

Metallicities of LAMOST-MRS young stars are estimated based on local thermodynamic equilibrium (LTE) models. But nonlocal thermodynamic equilibrium (NLTE) effects can significantly affect their spectra. NLTE effects may incur a bias of estimated metallicity with respect to $T_{\rm eff}$ (Xiang et al. 2022). To reduce the NLTE effects on the estimated metallicity values, we used a sixth-order polynomial to model the $T_{\rm eff}$ metallicity trend of the LAMOST-MRS young stellar sample. The dependency of metallicity on $T_{\rm eff}$ was mitigated by subtracting the fitted relation. We fitted the relation of metallicity and $T_{\rm eff}$ only using stars of $8.7 < R < 9.5$ kpc to avoid the effects of the radial metallicity gradients. Figure 2 shows the polynomial fit of the estimated $T_{\rm eff}$–metallicity trend. The distribution of stars on the $T_{\rm eff}$–$[{\rm M/H}]_{\rm corr}$ plane is also presented in Fig. 2, where the $[{\rm M/H}]_{\rm corr}$ is the metallicity after subtracting the trend. The figure shows that the final metallicity ($[{\rm M/H}]_{\rm corr}$) does not vary with $T_{\rm eff}$ after subtracting the mean trend. The metallicity used is the corrected metallicity ($[{\rm M/H}]_{\rm corr}$) in the following context.

3. Radial metallicity gradients of mono-temperature young stellar populations

In this section, we investigate the radial metallicity gradients of mono-temperature stellar populations. We divided stars from

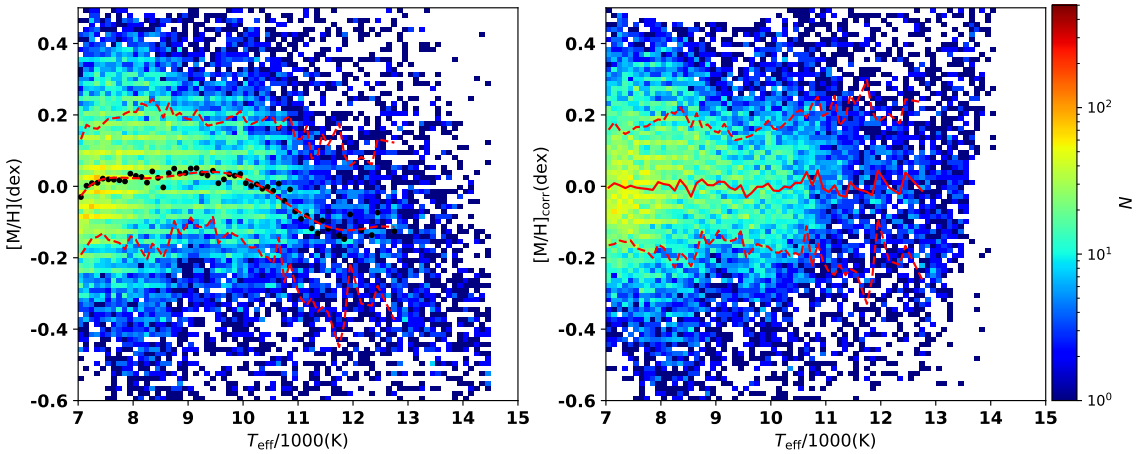

Fig. 2. Stellar number density distributions on the effective temperature and metallicity planes. The left panel displays the relation between the estimated metallicity and $T_{\rm eff}$ (black symbols) and their corresponding polynomial fit (red solid line) for the LAMOST-MRS young stellar sample. The black symbol represents the mean estimated metallicity and $T_{\rm eff}$ in each $T_{\rm eff}$ bin with a $\Delta_{T_{\rm eff}}$ of 100 K. The dashed red lines represent the corresponding standard deviations of the metallicity in each $T_{\rm eff}$ bin. Additionally, the stellar number density distribution on the $T_{\rm eff}$-[M/H] plane is plotted in the left panel. The right panel shows the stellar number density distribution on the $T_{\rm eff}$-[M/H]$_{\rm corr}$ plane. The solid and dashed red lines represent the mean corrected metallicity values and the corresponding standard deviations of the metallicity in each $T_{\rm eff}$ bin, respectively.

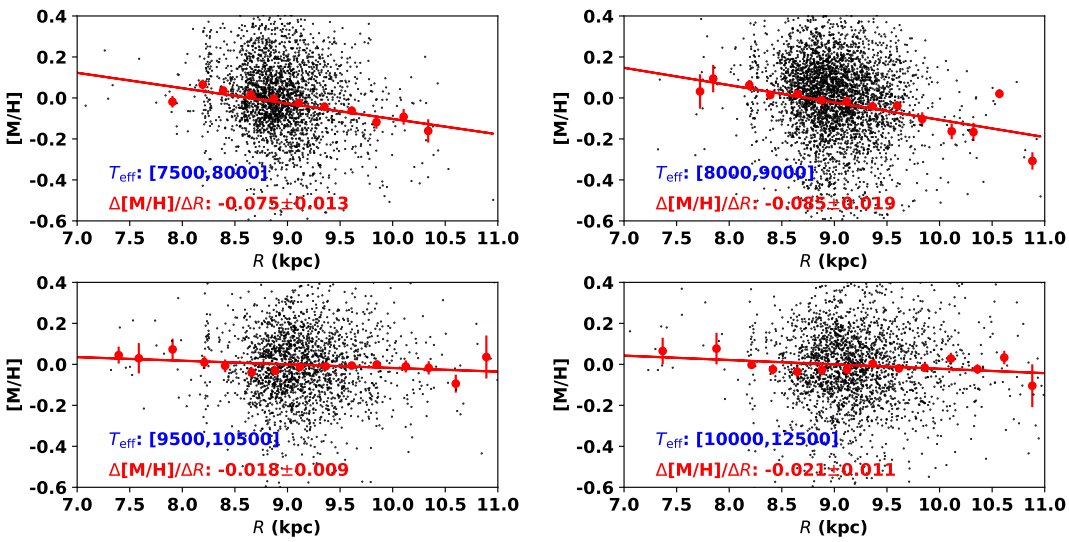

Fig. 3. Radial metallicity gradients of these four mono-temperature stellar populations. The red symbols represent the median metallicity values in individual radial bins. The line in red represents the linear regression over the red symbols. The temperature range of each stellar population, the slope of the linear fit (the radial metallicity gradient), and its associated uncertainty are marked in the bottom left panel.

the LAMOST-MRS stellar sample into different stellar populations in four effective temperature bins: 7500 < $T_{\rm eff}$ < 8000 K, 8500 < $T_{\rm eff}$ < 9000 K, 9500 < $T_{\rm eff}$ < 10 500 K, and 10 000 < $T_{\rm eff}$ < 12 500 K. We discarded stars with 9000 < $T_{\rm eff}$ < 9500 K because the Hα lines of these stars are not sensitive to $T_{\rm eff}$, which leads to large uncertainties as to the measured metallicities. In each temperature bin, we further divided stars into a small radial annulus of 0.25 kpc. Bins containing fewer than three stars were discarded. We performed linear regression on the metallicity as a function of the Galactic radius R. The slope was adopted as the radial metallicity gradient. Figure 3 shows the fitting results for these four mono-temperature stellar populations. As shown in the figure, a linear regression captures the trend between the metallicity and Galactic radius R well.

The radial metallicity gradient of the Galactic disk plays an important role in the study of Galactic chemical and dynamical evolution histories. It is also a fundamental input parameter in any models of Galactic chemical evolution. Previous studies on the radial metallicity gradient of the Galactic disk using different tracers (including OB stars by Daflon & Cunha 2004; Cepheid variables by Andrievsky et al. 2002; Luck et al. 2006; H II regions by Balser et al. 2011; OCs by Chen et al. 2003; Magrini et al. 2009; planetary nebulae by Costa et al. 2004; Henry et al. 2010; FGK dwarfs by Katz et al. 2011; Cheng et al. 2012; Boeche et al. 2013; red giant stars by Hayden et al. 2014; Boeche et al. 2014; and red clump stars by Huang et al. 2015) have presented that the Galactic disk has a negative radial metallicity gradient, which generally supports an inside-out disk-forming scenario. The variations of the radial metallicity gradient with stellar age (τ) have also been investigated by Xiang et al. (2015) and Wang et al. (2019) using main-sequence turn-off (MSTO) stars and other works (e.g. Yu et al. 2012; Casagrande et al. 2011; Toyouchi & Chiba 2018; Vickers et al. 2021). Wang et al. (2019) found that radial metallicity gradients

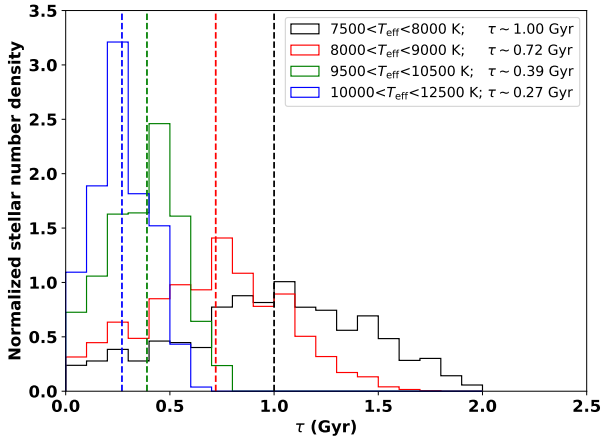

Fig. 4. Age distributions of stars within the metallicity range of −0.5 dex and 0.5 dex in these four effective temperature bins of $7500 < T_{\rm eff} < 8000$ K, $8500 < T_{\rm eff} < 9000$ K, $9500 < T_{\rm eff} < 10\,500$ K, and $10\,000 < T_{\rm eff} < 12\,500$ K predicted by the PARSEC isochrones. The median ages are over-plotted with dashed lines. The effective temperature ranges and median ages for each bin are marked in the top right corner of the figure.

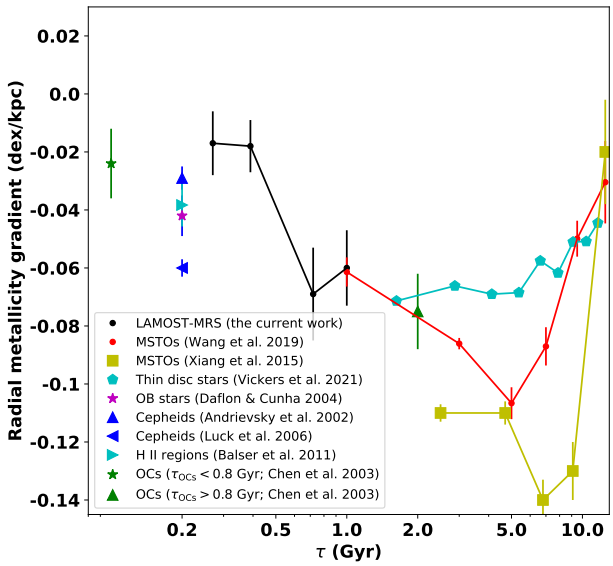

Fig. 5. Radial metallicity ([M/H]/[Fe/H]) gradient variations with stellar ages of the LAMOST-MRS young stellar sample in this work and those presented by Wang et al. (2019), Xiang et al. (2015), and Vickers et al. (2021). Radial metallicity gradients estimated using young objects (OB stars, Cepheid variables, H II regions, and OCs) from previous works are also shown using different symbols as labelled in the figure. We note that the x-axis is logarithmic.

steepen with increasing age at $\tau < 4$ Gyr, reach a maximum at $4 < \tau < 6$ Gyr , and then flatten with age. Xiang et al. (2015) also found a similar trend of radial metallicity gradients with stellar ages. Vickers et al. (2021) found that radial metallicity gradients generally grow shallower for the oldest stars. They did not detect the inflexion point of radial metallicity gradients. The possible reason may be the use of a guiding centre radius rather than the Galactocentric radius by Vickers et al. (2021) as they estimate radial metallicity gradients. However, the relation of the radial metallicity gradient with stellar age for the youngest stellar populations ($\tau < 2$ Gyr) was not investigated in these works due to the inaccuracy of the estimated stellar ages for the youngest stars.

For the youngest main-sequence stars, the stellar age has a tight relation with the effective temperature. We derived median stellar ages for these four mono-temperature stellar populations according to the PAdova and TRieste Stellar Evolution Code (PARSEC) isochrones (Bressan et al. 2012). Age distributions in these four effective temperature bins with the metallicity range of −0.5 dex and 0.5 dex (similar to the metallicity coverage of our sample) predicted by the PARSEC isochrones are shown in Fig. 4. The median ages are 1.00 Gyr, 0.72 Gyr, 0.39 Gyr, and 0.27 Gyr in these four effective temperature bins of $7500 < T_{\rm eff} < 8000$ K, $8500 < T_{\rm eff} < 9000$ K, $9500 < T_{\rm eff} < 10\,500$ K, and $10\,000 < T_{\rm eff} < 12\,500$ K, respectively.

Figure 5 shows the variations of radial metallicity gradients with the stellar ages of the LAMOST-MRS young stellar sample by us, the stellar ages of MSTO stars presented by Wang et al. (2019), and Xiang et al. (2015). Radial metallicity gradients estimated using young objects (including OB stars, Cepheid variables, H II regions, and OCs) are also over-plotted in the figure. We assumed a mean age of 0.2 Gyr for OB stars, Cepheid variables, and H II regions. Chen et al. (2003) divided their OCs into two age bins: $\tau < 0.8$ Gyr and $\tau > 0.8$ Gyr. We assumed a mean age of 0.1 Gyr and 2 Gyr following Chen et al. (2003). Radial metallicity gradients estimated using our LAMOST-MRS young stellar sample are well aligned with those values estimated using other young objects of previous works (Daflon & Cunha 2004; Andrievsky et al. 2002; Luck et al. 2006; Balser et al. 2011; Chen et al. 2003) within the uncertainties of the measurements. We find that radial metallicity gradients of young stellar populations ($\tau < 2$ Gyr) steepen as their age increases (with a gradient of $\sim$−0.055 dex kpc^{-1} Gyr^{-1}) within the uncertainty of our estimates. Yu et al. (2012) explored radial metallicity gradients across a range of effective temperatures and found that the gradient for stars with $T_{\rm eff} \sim 6500$ K was steeper than for those with $T_{\rm eff} \sim 7000$ K. Their relation of effective temperatures and metallicity gradients is consistent with our result. Our result is also consistent with those of Wang et al. (2019) and Xiang et al. (2015), who also found that the radial metallicity gradients decrease with increasing stellar age for young stellar populations ($1.5 < \tau < 4$ Gyr). Our results extend the relationship between the radial metallicity gradient and stellar age to $\tau < 1.5$ Gyr compared to Wang et al. (2019) and Xiang et al. (2015).

4. Azimuthal metallicity distributions of mono-temperature stellar populations

This section aims to investigate the azimuthal metallicity distributions of different mono-temperature stellar populations, as stipulated in Section 3. After these populations were divided initially, we then further divided these four mono-temperature stellar populations into different X–Y bins with a bin size of 0.1×0.1 kpc. This chosen spatial bin size aims to strike a balance between spatial resolution and the number of stars in each bin, with a preference for higher spatial resolution and a larger number of stars in each bin. Figure A.1 displays the distributions of stellar numbers in all X–Y bins. The typical uncertainties of X and Y are 0.0114 kpc and 0.0055 kpc, respectively, which are much smaller than the bin size of 0.1 kpc. To better visualise the azimuthal variation, we subtracted the mean radial metallicity gradient as measured in the previous section. We introduced a new metallicity scale denoted as the 'metallicity excess', Δ[M/H] = [M/H] − [M/H]$_{\rm R}$, where

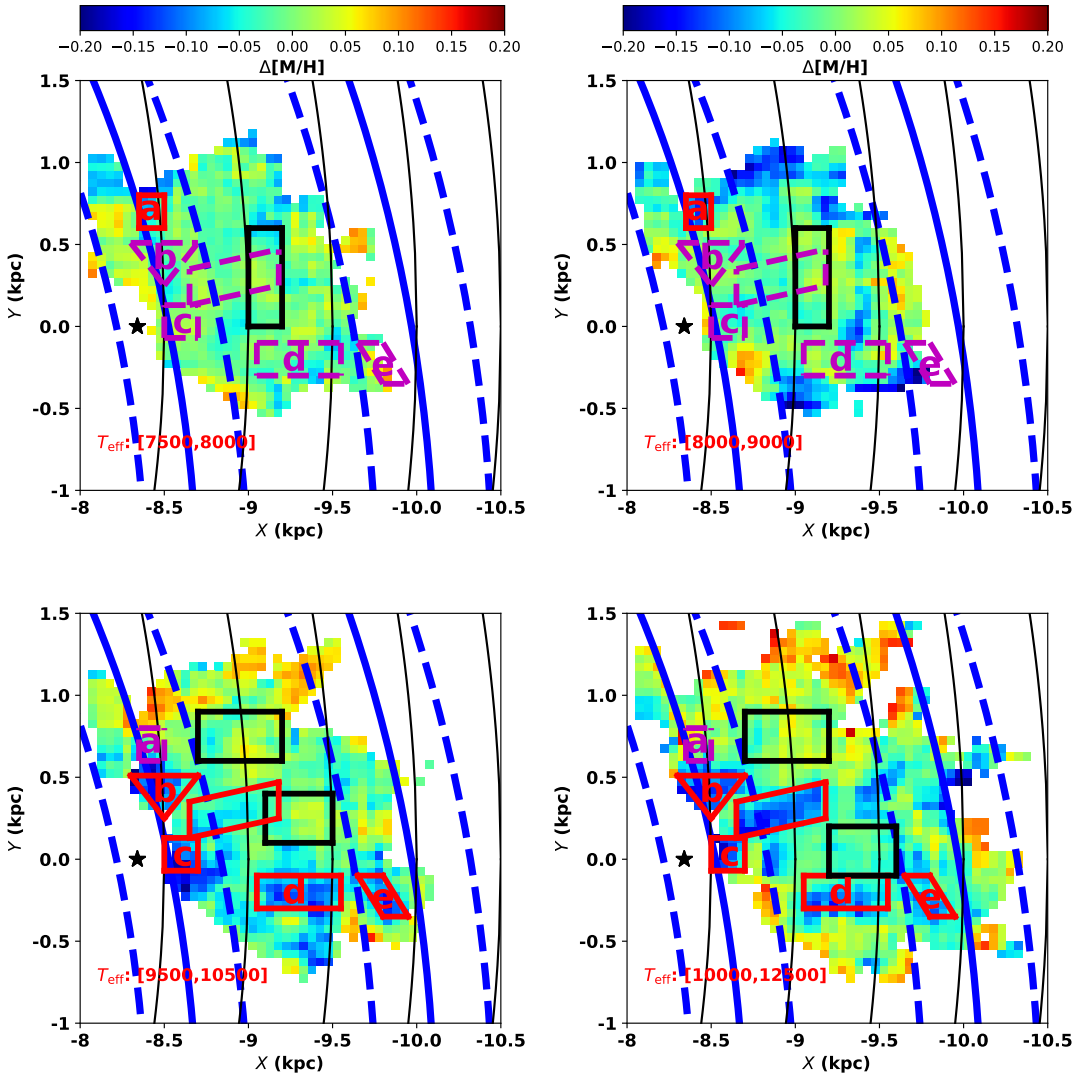

Fig. 6. Metallicity excess distributions after subtracting radial metallicity gradients for these four mono-temperature stellar populations, binned by 0.1×0.1 kpc on the X–Y plane. Bins that contained fewer than eight stars were discarded. The minimum number of stars in each bin was selected to ensure that the median metallicity excess uncertainties produced in these bins could distinguish the metal-poor substructures from other regions. The positions at R = 8.5, 9.0, 9.5, 10.0, and 10.5 kpc are marked with black arcs. The black star symbol indicates the position of the Sun. The centre and 1σ width of the spiral arms are shown by solid and dashed blue lines in all panels. Regions framed in red lines and dashed magenta lines indicate the spatial positions of these five metal-poor substructures (labelled by a, b, c, d, and e). A region framed by red lines means that it is a real metal-poor substructure of this mono-temperature stellar population. The region framed by dashed magenta lines is a corresponding region of metal-poor substructure in other mono-temperature stellar populations. Control regions are framed in black lines.

$[\mathrm{M/H}]_{\mathrm{R}}$ is the median metallicity in each R bin with a bin scale of 0.5 kpc. In each X and Y bin, we estimated the mean $\Delta[\mathrm{M/H}]$ and its associated dispersion ($\sigma[\mathrm{M/H}]$), as well as their uncertainties.

4.1. Global statistics

Figure 6 shows the azimuthal metallicity excess ($\Delta[\mathrm{M/H}]$) distributions of these four mono-temperature stellar populations on the X–Y plane, which shows significant inhomogeneities on the bin scale of 0.1×0.1 kpc. The difference of metallicity excess spans almost 0.4 dex (ranging from −0.2 dex to 0.2 dex). The dispersions of the (median) metallicity excess (shown in Fig. 6) are 0.04 dex, 0.058 dex, 0.057 dex, and 0.066 dex for the stellar populations with effective temperature coverage of $7500 < T_{\rm eff} < 8000$ K, $8500 < T_{\rm eff} < 9000$ K, $9500 < T_{\rm eff} < 10\,500$ K, and $10\,000 < T_{\rm eff} < 12\,500$ K, respectively, as shown in Fig. 7. The metallicity excess dispersion increases as the temperature increases.

We computed the two-point correlation function of metallicity excess for these four mono-temperature stellar populations to quantify the scale length associated with the observed metallicity inhomogeneity with the same method of Kreckel et al. (2020). The 50% level scale length is ~0.05 kpc, which is smaller than our spatial bin size of 0.1 kpc. The result suggests that the scale length of metallicity inhomogeneity is smaller than 0.1 kpc. This scale length is much smaller than 0.5-1.0kpc predicted by Krumholz & Ting (2018) and 0.3 kpc (50% level) estimated by Kreckel et al. (2020) using HII regions in external galaxies. It is possible that their results in external galaxies may not be directly applicable to the MW. The origin of the chemical inhomogeneities observed in this paper may differ from those observed in external galaxies. The scale length is consistent with that of De Cia et al. (2021), who suggest that pristine gas falling

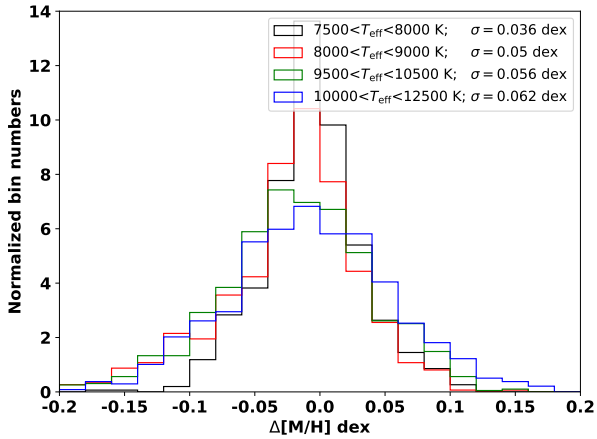

Fig. 7. Bin number density distributions of metallicity excess in Fig. 6 of these four mono-temperature stellar populations. The effective temperature ranges and dispersions of these four distributions are marked in the top right corner of the figure.

into the 'Galactic disk' can produce chemical inhomogeneities on the scale of tens of parsecs.

To check the reliability of metallicity inhomogeneities, we study the distributions of metallicity excess uncertainties ($\Delta[\mathrm{M/H}]_{\mathrm{err}}$) in Fig. A.2. We note that $\Delta[\mathrm{M/H}]_{\mathrm{err}}$ are mostly smaller than 0.1 dex (with median values of 0.030, 0.039, 0.042, and 0.048 dex for stellar populations of $7500 < T_{\mathrm{eff}} < 8000$ K, $8500 < T_{\mathrm{eff}} < 9000$ K, $9500 < T_{\mathrm{eff}} < 10\,500$ K, and $10\,000 < T_{\mathrm{eff}} < 12\,500$ K, respectively), which is much smaller than the difference of metallicity excess shown in Fig. 6. The comparison between Figs. 6 and A.2 suggests that the observed azimuthal metallicity inhomogeneities are reliable.

Figures 6 and 7 not only show the azimuthal metallicity inhomogeneity, but also its variations with effective temperature. Azimuthal metallicity inhomogeneities (a larger metallicity dispersion means a larger metallicity inhomogeneity) of young stellar populations ($T_{\mathrm{eff}} > 8000$ K) are much larger than that of the old stellar population ($T_{\mathrm{eff}} < 8000$ K).

In addition to metallicity excess distributions, we also investigate the spatial distributions of metallicity excess dispersions. Figures A.3 and A.4 show the spatial distributions of metallicity excess dispersion and its associated uncertainty. From Fig. A.3, we can find inhomogeneities of metallicity dispersion distributions for the four mono-temperature stellar populations. Inhomogeneities of young stellar populations ($T_{\mathrm{eff}} > 8000$ K) are much larger than those of the old stellar population ($T_{\mathrm{eff}} < 8000$ K). Metallicity dispersion uncertainties shown in Fig. A.4 are much smaller than the difference of metallicity dispersions shown in Fig. A.3, which suggests that observed azimuthal metallicity dispersion distributions in Fig. A.3 are reliable.

4.2. Metal-poor substructures

From Figs. 6 and A.3, we observe several metal-poor substructures with large metallicity dispersions. In the old stellar population ($8000 < T_{\mathrm{eff}} < 9000$ K), we identify one metal-poor substructure (labelled 'a' in Fig. 6), which is not found in the stellar populations of $T_{\mathrm{eff}} > 9500$ K. The metallicity of this metal-poor substructure is smaller than its nearby regions by ~0.1 dex. The metal-poor substructure is also found in the stellar population of $7500 < T_{\mathrm{eff}} < 8000$ K, while it is much weaker. In the younger stellar population ($9500 < T_{\mathrm{eff}} < 12\,500$ K), there are four metal-poor regions labelled 'b', 'c', 'd', and 'e' in Fig. 6, which are not found in the two old stellar populations. The metallicities of these four regions are also smaller than their nearby regions by ~0.1 dex. The spatial sizes of a, b, c, d, and e substructures are ~0.7×0.2, 0.3×0.2, 0.8×0.2, 0.4×0.1 kpc, and 0.1×0.4 kpc, respectively.

Azimuthal metallicity variations with spatial positions may be tracked along spiral arms (e.g. Khoperskov et al. 2018; Poggio et al. 2022). We compared the azimuthal metallicity distributions, especially those of the five identified metal-poor substructures, with the spiral arms (shown as the solid and dashed blue line, indicating from left to right the segments of the Local (Orion) arm and the Perseus arm) determined using high-mass star-forming regions by Reid et al. (2019). From Fig. 6, we find that metallicity distributions of these four mono-temperature stellar populations do not track the expected locations of spiral arms, similar to the results presented by Hawkins (2023). Hawkins (2023) mapped out azimuthal metallicity distributions using LAMOST OBAF young stars selected from LAMOST low-resolution spectra by Xiang et al. (2022). However, our detailed azimuthal metallicity patterns have large differences compared to those of Hawkins (2023). We cross-matched the LAMOST-MRS young stellar sample with their OBAF stellar sample and plotted azimuthal metallicity distributions using the common stars. For these common stars, the azimuthal metallicity distributions are similar either using the metallicity of the LAMOST-MRS or LAMOST OBAF sample, which are also similar to the results presented here. Different fractions and the origin of contaminations from cold stars of the two samples may be responsible for the difference between our results and those of Hawkins (2023).

In Fig. A.5 we show the normalised metallicity excess distributions of these five metal-poor regions (a, b, c, d, and e regions) and those of control regions (framed in black lines). The skewnesses of the metallicity distributions were also estimated. All of these skewnesses are smaller than zero, suggesting that metallicity distributions, both in the metal-poor regions and control regions, have metal-poor tails. Metal-poor substructures contain a larger fraction of metal-poor stars and have a much smaller skewness compared to control regions.

5. The ISM mixing process

Azimuthal metallicity distributions mapped out by the LAMOST-MRS stellar sample presented in Sect. 4 suggest that there are significant azimuthal metallicity inhomogeneities. Similarly, the azimuthal metallicity distributions of the ISM (Balser et al. 2011, 2015; De Cia et al. 2021), Cepheid variable stars (Pedicelli et al. 2009), and OCs (Davies et al. 2009; Fu et al. 2022) in the MW also show significant azimuthal metallicity inhomogeneities. Azimuthal metallicity inhomogeneities of external spiral galaxies are also found through investigating the metallicity of H II regions (Ho et al. 2017, 2018; Kreckel et al. 2019, 2020). These observed azimuthal metallicity inhomogeneities, both in the MW and external spiral galaxies, suggest that the ISM is not well mixed.

High-velocity clouds infalling into the Galactic disk from the Galaxy halo are metal-poor, with metallicities ranging from 0.1 to 1.0 solar metal (Fox & Dave 2017; Wright et al. 2021; De Cia et al. 2021). High-velocity clouds can be generated by the 'galactic fountain' cycle and other gas accretion processes. Intermediate-velocity clouds are also the main observational manifestations of the ongoing galactic fountain cycle (Wakker & van Woerden 1997). However, unlike high-velocity

clouds, intermediate-velocity clouds are nearby systems and have near or solar metallicity. These five metal-poor substructures found in the current paper have smaller mean metallicity values and larger dispersions. They also contain a larger fraction of metal-poor stars than other Galactic disk regions. These results suggest that these five metal-poor substructures may be associated with high-velocity clouds, which infall into the Galactic disk from the Galactic halo. These high-velocity clouds are not quickly well mixed with the ISM of the Galactic disk after they infall into the Galactic disk, thus they have time to produce stars, which are more metal-poor than stars born in the pre-existing Galactic disk ISM. As a result, the metallicity dispersions in the locations of these high-velocity clouds are larger than those of other regions.

As shown in Sect. 4, the azimuthal metallicity inhomogeneity and dispersion increase as temperature increases. Five metal-poor (large metallicity dispersion) substructures are found. Four of these substructures are only found in the metallicity distributions of young stellar populations ($T_{\rm eff} > 9500$ K). These metal-poor substructures of the stellar population with $9500 < T_{\rm eff} < 10\,500$ K (with a median stellar age of 0.39 Gyr) may suggest that the corresponding high-velocity clouds had infalled into the Galactic disk 0.39 Gyr ago. Similarly, these metal-poor substructures of $10\,000 < T_{\rm eff} < 12\,500$ K (with a median stellar age of 0.27 Gyr) may suggest that these corresponding high-velocity clouds had not been well mixed into the Galactic disk ISM before 0.27 Gyr. In conclusion, these high-velocity clouds infalling into the Galactic disk from the Galactic halo are not well mixed with the pre-existing Galactic disk ISM within 0.12 Gyr (0.39−0.27 Gyr).

It is noted that the d metal-poor substructure of the stellar population with $10\,000 < T_{\rm eff} < 12\,500$ K move ~0.1 kpc on the X–Y plane compared to that of $9500 < T_{\rm eff} < 10\,500$ K. This may be the consequence of the velocity difference between infalling high-velocity clouds and stars or the ISM of the Galactic disk. A velocity difference of ~0.82 km s^{-1} is needed to move 0.1 kpc within 0.12 Gyr, which is reasonable.

The other metal-poor substructure is found in the metallicity distributions of old stellar populations ($T_{\rm eff} < 9000$ K), suggesting that the corresponding high-velocity cloud had not sufficiently mixed with the Galactic disk ISM before 0.72 Gyr (the median age of the stellar population with $8000 < T_{\rm eff} < 9000$ K) and had infalled into the Galactic disk 1.0 Gyr (the median age of the stellar population with $7500 < T_{\rm eff} < 8000$ K) ago. The results suggest that the high-velocity cloud is not well mixed into the Galactic disk ISM within 0.28 Gyr. This substructure is not found in the metallicity distributions of young stellar populations, suggesting that this high-velocity cloud had been well mixed into the Galactic disk ISM 0.39 Gyr ago.

6. Summary

In this work, we use the LAMOST-MRS young stellar sample with an accurate effective temperature and metallicity to investigate the radial metallicity gradients and azimuthal metallicity distributions of different stellar populations with varying effective temperatures (or ages). The estimated radial metallicity gradient ranges from −0.015 dex/kpc to −0.07 dex/kpc, which decreases as the effective temperature decreases (or when the stellar age increases). The result is consistent with those of Xiang et al. (2015) and Wang et al. (2019), who also found that the radial metallicity gradients decrease with increasing stellar age for young stellar populations ($1.5 < \tau < 4$ Gyr). Our results extended their study of the relation between the radial metallicity gradient and the stellar age to $\tau < 1.5$ Gyr.

After subtracting radial metallicity gradients on the X–Y plane, the azimuthal metallicity distributions of these four mono-temperature stellar populations show significant metallicity inhomogeneities, which is consistent with previous studies of azimuthal metallicity distributions of the MW (Balser et al. 2011, 2015; De Cia et al. 2021; Pedicelli et al. 2009; Davies et al. 2009) and external spiral galaxies (Ho et al. 2017, 2018; Kreckel et al. 2019, 2020). The result suggests that the ISM is not well mixed at any time.

We find five metal-poor substructures with sizes of ~0.2–1.0 kpc, and the metallicities of which are smaller than their nearby regions by ~0.1 dex. These metal-poor substructures may be associated with high-velocity clouds infalling into the Galactic disk from the Galactic halo. According to the results of stellar populations at different ages, we suggest that high-velocity clouds infalling into the Galactic disk from the Galactic halo are not well mixed with the pre-existing Galactic disk ISM within 0.3 Gyr.

The size and spatial distribution of our stellar sample are mainly limited by the faint limiting magnitude (15 mag in g-band) of the LAMOST MRS survey. Future large-scale spectroscopic surveys, including SDSS-V (Kollmeier et al. 2017; Zari et al. 2021) and 4MOST (de Jong et al. 2022), are expected to improve our work by enlarging the sample size and spatial coverage.

Acknowledgements. We appreciate the helpful comments of the anonymous referee. This work was funded by the National Key R&D Program of China (No. 2019YFA0405500) and the National Natural Science Foundation of China (NSFC Grant No. 12203037, No. 12222301, No. 12173007 and No. 11973001). We acknowledge the science research grants from the China Manned Space Project with NO. CMS-CSST-2021-B03. We used data from the European Space Agency mission *Gaia* (http://www.cosmos.esa.int/gaia), processed by the *Gaia* Data Processing and Analysis Consortium (DPAC; see http://www.cosmos.esa.int/web/gaia/dpac/consortium). Guoshoujing Telescope (the Large Sky Area Multi-Object Fiber Spectroscopic Telescope LAMOST) is a National Major Scientific Project built by the Chinese Academy of Sciences. Funding for the project has been provided by the National Development and Reform Commission. LAMOST is operated and managed by the National Astronomical Observatories, Chinese Academy of Sciences.

References

Andrievsky, S. M., Kovtyukh, V. V., Luck, R. E., et al. 2002, A&A, 381, 32
Bailer-Jones, C. A. L., Rybizki, J., Fouesneau, M., Demleitner, M., & Andrae, R. 2021, AJ, 161, 147
Balser, D. S., Rood, R. T., Bania, T. M., & Anderson, L. D. 2011, ApJ, 738, 27
Balser, D. S., Wenger, T. V., Anderson, L. D., & Bania, T. M. 2015, ApJ, 806, 199
Boeche, C., Siebert, A., Piffl, T., et al. 2013, A&A, 559, A59
Boeche, C., Siebert, A., Piffl, T., et al. 2014, A&A, 568, A71
Bressan, A., Marigo, P., Girardi, L., et al. 2012, MNRAS, 427, 127
Casagrande, L., Schönrich, R., Asplund, M., et al. 2011, A&A, 530, A138
Chen, L., Hou, J. L., & Wang, J. J. 2003, AJ, 125, 1397
Cheng, J. Y., Rockosi, C. M., Morrison, H. L., et al. 2012, ApJ, 746, 149
Costa, R. D. D., Uchida, M. M. M., & Maciel, W. J. 2004, A&A, 423, 199
Daflon, S., & Cunha, K. 2004, ApJ, 617, 1115
Davies, B., Origlia, L., Kudritzki, R.-P., et al. 2009, ApJ, 696, 2014
De Cia, A., Jenkins, E. B., Fox, A. J., et al. 2021, Nature, 597, 206
de Jong, R. S., Bellido-Tirado, O., Brynnel, J.G., et al. 2022, in Ground-based and Airborne Instrumentation for Astronomy IX, eds. C. J. Evans, J. J. Bryant, & K. Motohara, 12184, 1218414
Fox, A., & Davé, R. 2017, Astrophys. Space Sci. Lib., 430
Frankel, N., Rix, H.-W., Ting, Y.-S., Ness, M., & Hogg, D. W. 2018, ApJ, 865, 96
Frankel, N., Sanders, J., Ting, Y.-S., & Rix, H.-W. 2020, ApJ, 896, 15
Fu, X., Bragaglia, A., Liu, C., et al. 2022, A&A, 668, A4

Hawkins, K. 2023, MNRAS, in press, https://doi.org/10.1093/mnras/stad1244
Hayden, M. R., Holtzman, J. A., Bovy, J., et al. 2014, AJ, 147, 116
Henry, R. B. C., Kwitter, K. B., Jaskot, A. E., et al. 2010, ApJ, 724, 748
Ho, I. T., Seibert, M., Meidt, S. E., et al. 2017, ApJ, 846, 39
Ho, I. T., Meidt, S. E., Kudritzki, R.-P., et al. 2018, A&A, 618, A64
Huang, Y., Liu, X.-W., Zhang, H.-W., et al. 2015, Res. Astron. Astrophys., 15, 1240
Katz, D., Soubiran, C., Cayrel, R., et al. 2011, A&A, 525, A90
Khoperskov, S., Di Matteo, P., Haywood, M., & Combes, F. 2018, A&A, 611, L2
Kollmeier, J. A., Zasowski, G., Rix, H. W., et al. 2017, ArXiv e-prints [arXiv:1711.03234]
Kreckel, K., Ho, I. T., Blanc, G. A., et al. 2019, ApJ, 887, 80
Kreckel, K., Ho, I. T., Blanc, G. A., et al. 2020, MNRAS, 499, 193
Krumholz, M. R., & Ting, Y.-S. 2018, MNRAS, 475, 2236
Kubryk, M., Prantzos, N., & Athanassoula, E. 2015, A&A, 580, A126
Lian, J., Zasowski, G., Hasselquist, S., et al. 2022, MNRAS, 511, 5639
Luck, R. E., Kovtyukh, V. V., & Andrievsky, S. M. 2006, AJ, 132, 902
Magrini, L., Sestito, P., Randich, S., & Galli, D. 2009, A&A, 494, 95
Matteucci, F. 2012, Chemical Evolution of Galaxies (Springer-Verlag Berlin Heidelberg)
Matteucci, F. 2021, A&A Rev., 29, 5
Minchev, I., & Famaey, B. 2010, ApJ, 722, 112
Pedicelli, S., Bono, G., Lemasle, B., et al. 2009, A&A, 504, 81
Poggio, E., Recio-Blanco, A., Palicio, P. A., et al. 2022, A&A, 666, L4
Reid, M. J., Menten, K. M., Brunthaler, A., et al. 2014, ApJ, 783, 130
Reid, M. J., Menten, K. M., Brunthaler, A., et al. 2019, ApJ, 885, 131
Schaller, G., Schaerer, D., Meynet, G., & Maeder, A. 1992, A&AS, 96, 269
Sun, W., Duan, X.-W., Deng, L., et al. 2021, ApJS, 257, 22
Tinsley, B. M. 1980, Fund Cosmic Phys., 5, 287
Toyouchi, D., & Chiba, M. 2018, ApJ, 855, 104
Vickers, J. J., Shen, J., & Li, Z.-Y. 2021, ApJ, 922, 189
Wakker, B. P., & van Woerden, H. 1997, ARA&A, 35, 217
Wang, C., Liu, X. W., Xiang, M. S., et al. 2019, MNRAS, 482, 2189
Wright, R. J., Lagos, C. d. P., Power, C., & Correa, C. A. 2021, MNRAS, 504, 5702
Xiang, M.-S., Liu, X.-W., Yuan, H.-B., et al. 2015, Res. Astron. Astrophys., 15, 1209
Xiang, M., Rix, H.-W., Ting, Y.-S., et al. 2022, A&A, 662, A66
Yu, J., Sellwood, J. A., Pryor, C., Chen, L., & Hou, J. 2012, ApJ, 754, 124
Zari, E., Rix, H. W., Frankel, N., et al. 2021, A&A, 650, A112
Zorec, J., & Royer, F. 2012, A&A, 537, A120

Appendix A: Additional figures

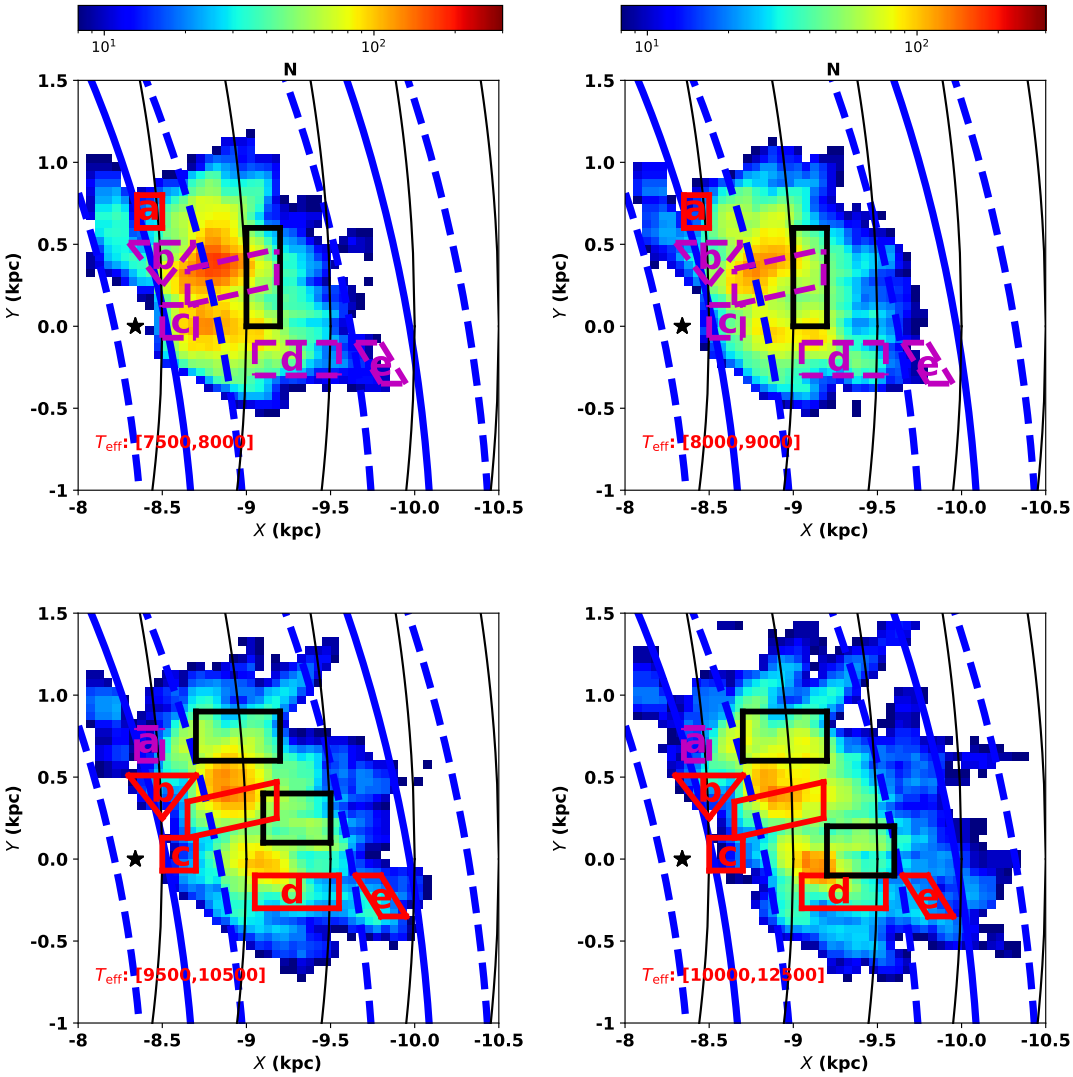

Fig. A.1. Same as Figure 6, but for the stellar number distributions.

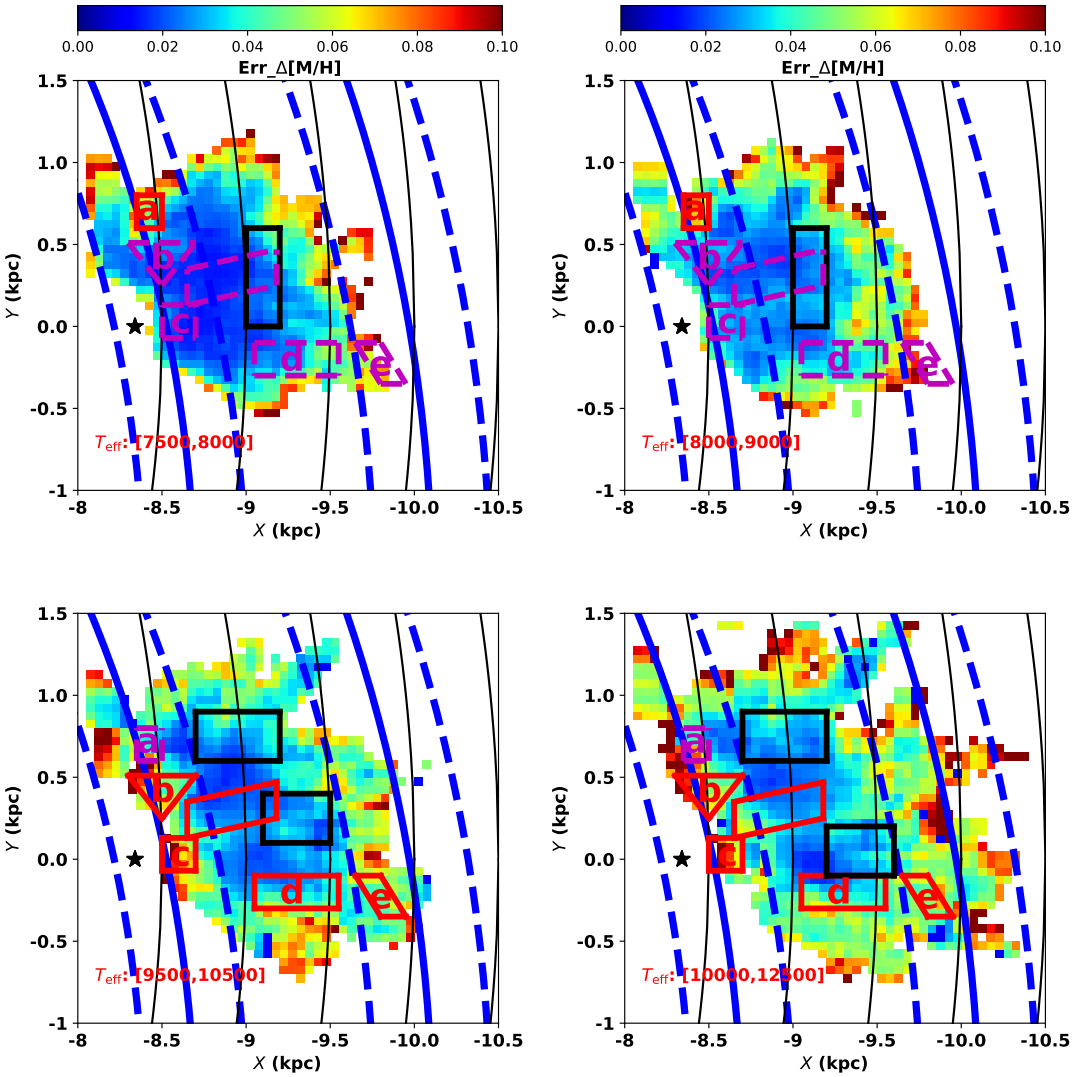

Fig. A.2. Same as Figure 6, but for the distributions of metallicity excess uncertainties.

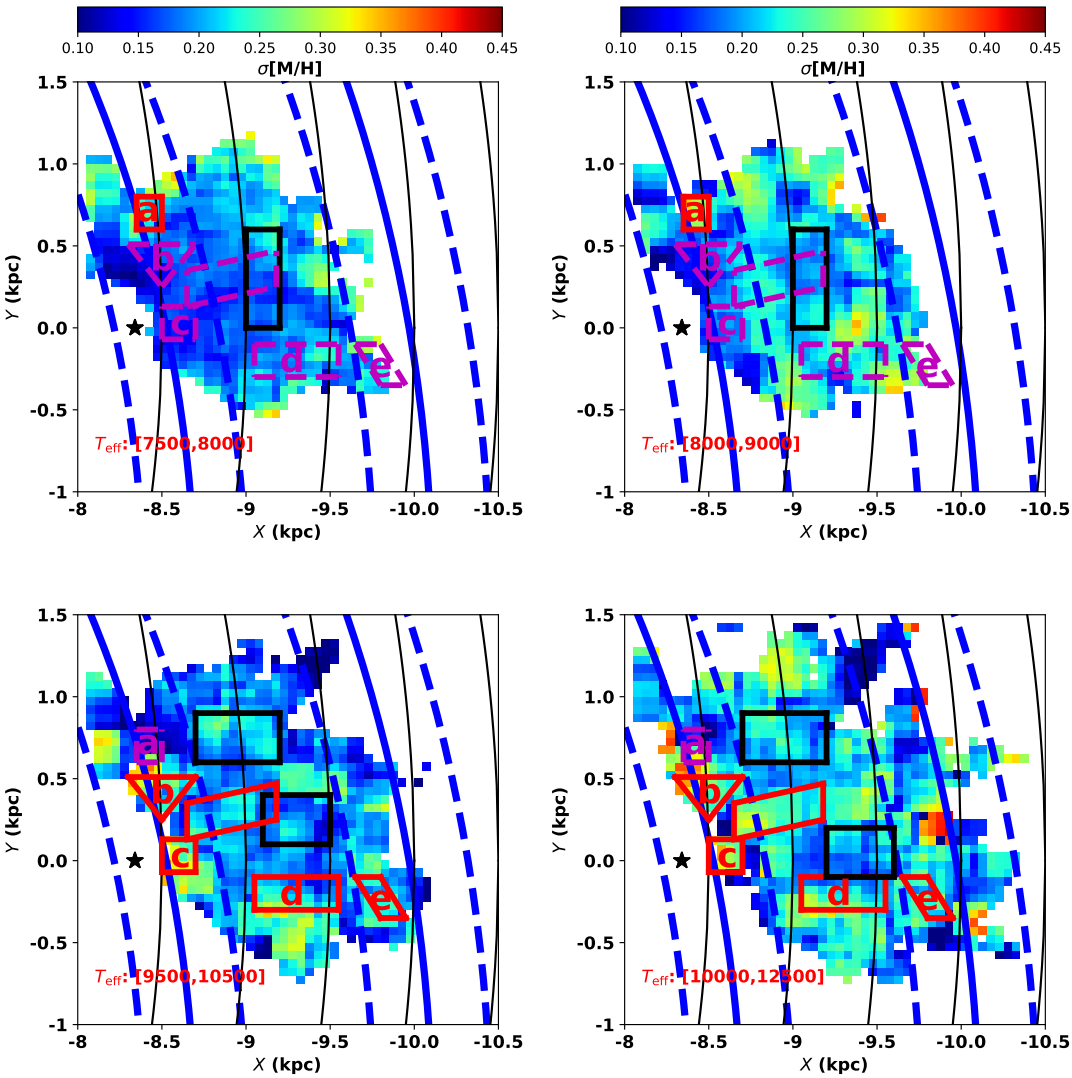

Fig. A.3. Same as Figure 6, but for the distributions of the dispersion of the metallicity excess.

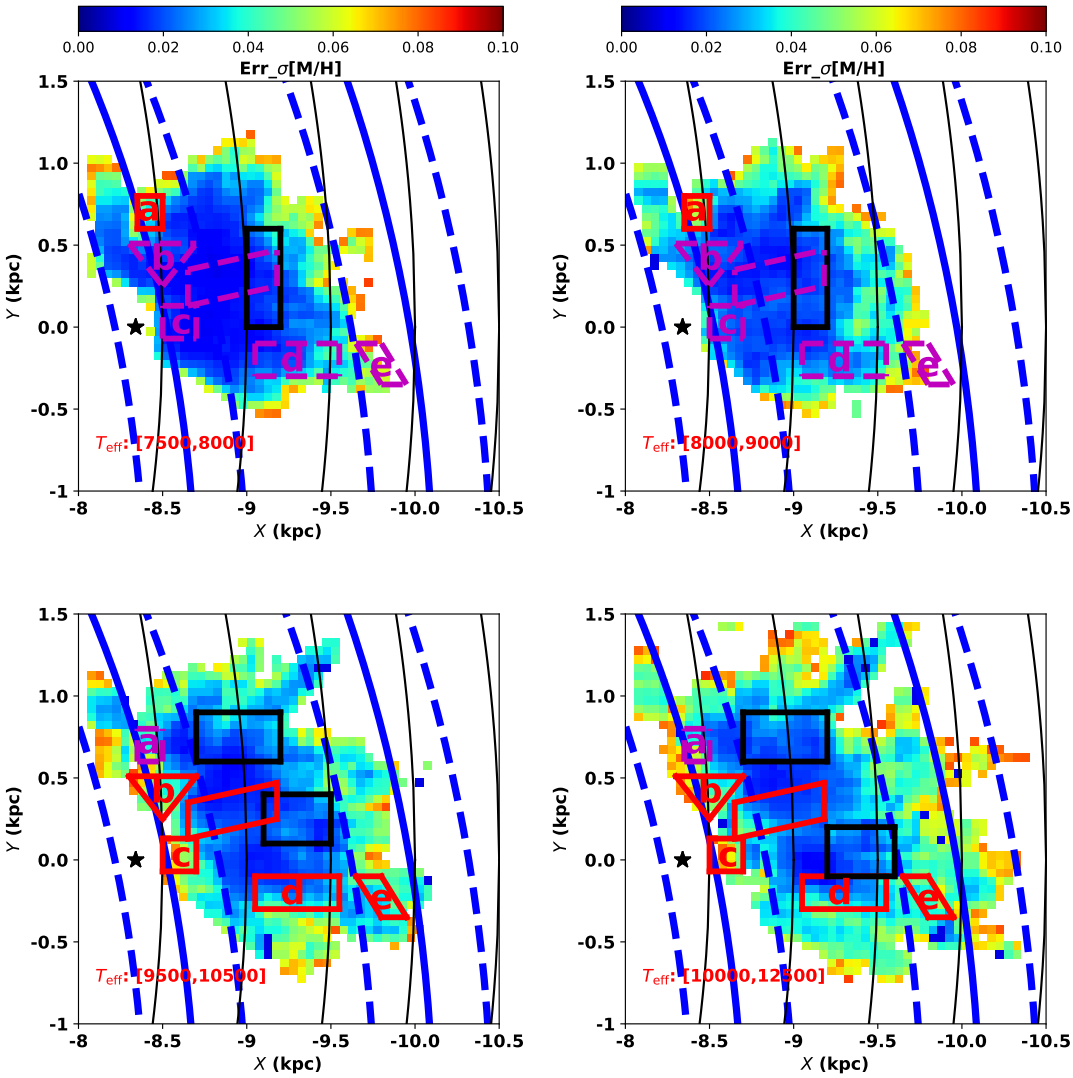

Fig. A.4. Same as Figure 6, but for the distributions of the metallicity excess dispersion's uncertainty.

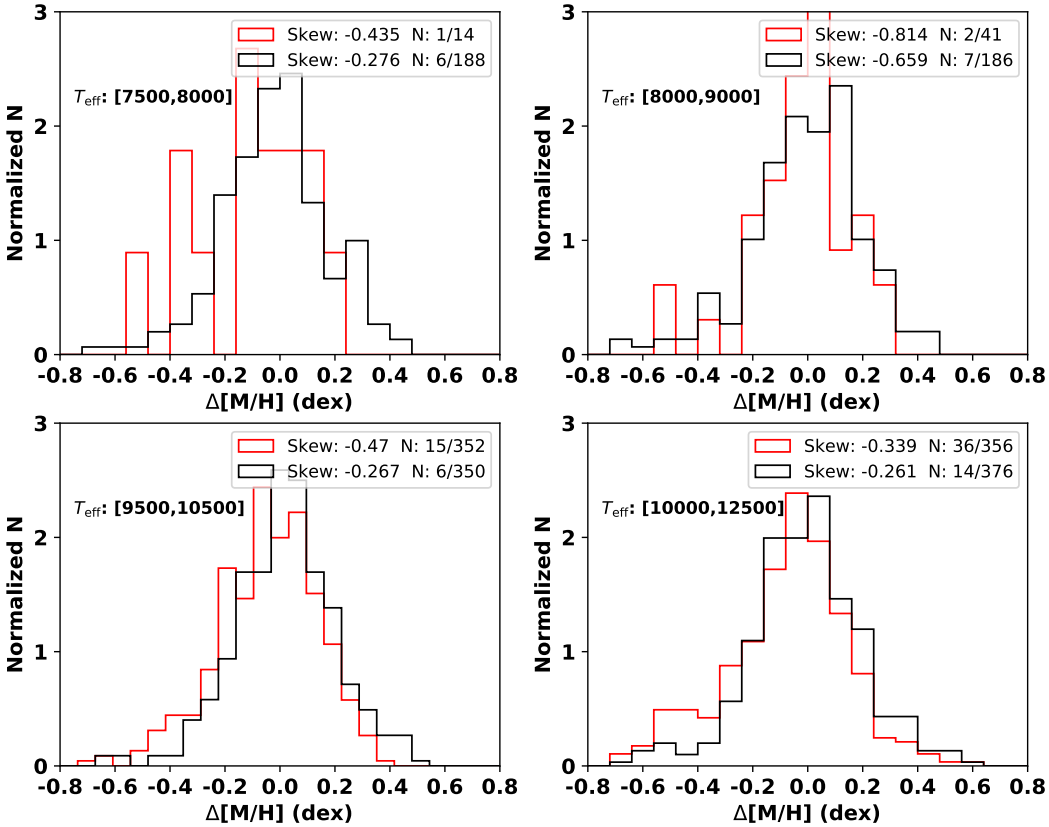

Fig. A.5. Metallicity excess distributions in metal-poor regions (red histogram) and their control regions (black histogram) of these four mono-temperature stellar populations. The skewness of these distributions is estimated and labelled in the top right corner of each panel. The total number and the number of stars with $[\mathrm{M/H}]_{\rm corr} < -0.4$ dex are also shown in the figure.